EDGE ARTICLE

Check for updates

Polyethyleneimine functionalized platinum superstructures: enhancing hydrogen evolution performance by morphological and interfacial control†

Guang-Rui Xu,‡[a] Juan Bai,‡[a] Jia-Xing Jiang, [ID][a] Jong-Min Lee [ID] *[b] and Yu Chen [ID] *[a]

The electrocatalytic hydrogen evolution reaction (HER) is a highly promising green method for sustainable and efficient hydrogen production. So far, Pt nanocrystals are still the most active electrocatalysts for the HER in acidic media, although a tremendous search for alternatives has been done in the past decade. In this work, we synthesize polyethyleneimine (PEI) functionalized Pt superstructures (Pt-SSs@PEI) with tetragonal, hierarchical, and branched morphologies with a facile wet chemical reduction method. A series of physical characterizations are conducted to investigate the morphology, electronic structure, surface composition, and formation mechanism of Pt-SSs@PEI. Impressively, the as-prepared Pt-SSs@PEI show an unprecedented onset reduction potential (+64.6 mV *vs.* reversible hydrogen electrode) for the HER in strong acidic media due to the protonation of $-NH_2$ groups in the PEI adlayers on the Pt surface, and they outperform all currently reported HER electrocatalysts. The work highlights a highly effective interface-engineering strategy for improving the electrocatalytic performance of Pt nanocrystals for the HER.

Introduction

Hydrogen is one of the most important green and renewable energy sources. Among the various methods for hydrogen production, electrochemical water splitting (EWS) is viewed as one of the simplest and most advanced approaches because of its inherent advantages, including stable output, no emissions, and high-purity of products.[1–3] The EWS device requires highly active and durable cathode electrocatalysts for the hydrogen evolution reaction (HER) to reduce the overpotential and increase the current density, which have a profound effect on the cost, efficiency, and lifetime of the EWS devices.[4,5] In acidic media, the HER has very fast reduction kinetics, which is 2–3 orders of magnitude higher than that obtained in alkaline media.[3] Although many non-precious metal-based nanocrystals show promising activity for the HER, their electrocatalytic performance is still insufficient for industrial applications, especially in acidic media.[6] So far, precious Pt is still considered as the best electrocatalyst for the HER in acidic media because of its extreme chemical inertness and near-zero overpotential, and it has been employed widely in EWS devices.[7,8]

In general, the electrocatalytic activity of Pt nanocrystals for the HER relies heavily on their morphology and chemical composition because of geometrical, electronic, and architectural effects. Like other electrochemical reactions, the HER is a structure-sensitive reaction. Thus, the geometrical structure of Pt nanocrystals affects their electrocatalytic activity for the HER. For example, the HER at the Pt(110) and Pt(100) surfaces obeys the Tafel–Volmer mechanism and the Heyrovsky–Volmer sequence in acidic media, respectively.[9] Meanwhile, the adsorption/dissociation energies of reactants highly relate to the chemical composition of Pt nanocrystals. Thus, the electrocatalytic activity of Pt nanocrystals for the HER can be improved by incorporating transition metals. For example, trimetallic PtFeCo nanotristars show composition-dependent HER activity because the interaction between Pt atoms and transition metal atoms can tune the surface electronic structure of Pt atoms.[10] Additionally, the HER is also an architecture-sensitive reaction. For example, the pine-shaped Pt nanoarray electrode shows improved HER performance compared to the planar Pt electrode because the three dimensional (3D) array morphology with a rough surface can facilitate the release of hydrogen gas bubbles due to the low gas bubble adhesion force.[11]

[a] Key Laboratory of Macromolecular Science of Shaanxi Province, Key Laboratory of Applied Surface and Colloid Chemistry (MOE), Shaanxi Key Laboratory for Advanced Energy Devices, School of Materials Science and Engineering, Shaanxi Normal University, Xi'an 710062, China. E-mail: ndchenyu@gmail.com

[b] School of Chemical and Biomedical Engineering, Nanyang Technological University, Singapore 637459, Singapore. E-mail: jmlee@ntu.edu.sg

Traditionally, it is believed that the clean/pristine surface of precious metal nanocrystals is necessary for high electrocatalytic activity. Recently, many investigations have demonstrated that the electrocatalytic performance (such as activity and selectivity) of precious metal nanocrystals also relies on their interfacial properties, besides morphology and chemical composition. Thus, functionalizing precious metal nanocrystals with organic ligands has become a new technological route for improving electrocatalytic performance.[12–30] For instance, calix[4]arene modified Pt nanocrystals show almost 100% selectivity for hydrogen electrooxidation in the presence of oxygen.[12,13] The cucurbit[6]uril functionalized Pt nanocrystals show an excellent anti-poisoning capability for methanol electrooxidation because of the peculiar interaction between the CO intermediate and the cucurbit[6]uril molecule.[14] The polyallylamine functionalized Pt nanodendrites show enhanced electrocatalytic activity and particular alcohol tolerance for oxygen electroreduction due to the modified electronic property and steric property of polyallylamine adlayers.[27]

According to the Nernst equation and reaction equation of the HER ($2H^+ + 2e^- \rightarrow H_2$), the onset reduction potential of the HER at Pt nanocrystals highly depends on the H^+ concentration on the Pt-electrolyte interface, implying that the electrocatalytic activity of the Pt nanocrystals for the HER can be improved by elevating the local H^+ concentration at the Pt–electrolyte interface. Recently, 3D hierarchical Pt superstructures with interconnected branches generally showed improved reactivity and long-term stability of electrochemical reactions due to the high specific surface area, good electrical connectivity, abundant twinned defect atoms, fast mass transfer, and less Ostwald ripening.[31–34] Thus, one can combine morphology control with interface control to boost the electrocatalytic performance of Pt nanocrystals for the HER. In this work, a simple wet chemical reduction method is proposed to successfully synthesize polyethyleneimine (PEI) functionalized Pt superstructures (Pt-SSs@PEI) with tetragonal, hierarchical, and branched morphologies. The HER at the Pt-SSs@PEI has an unprecedented onset reduction potential (+64.6 mV *vs.* reversible hydrogen electrode) in strong acidic media. The super activity of the Pt-SSs@PEI for the HER is attributed to the protonation of –NH$_2$ groups at the PEI adlayers on the Pt surface, which effectively elevates the local H^+ concentration at the electrode/solution interface.

Experimental section

Reagents and chemicals

PEI (Scheme S1,† MW = 70 000) was obtained from Sigma-Aldrich (Shanghai, China). Potassium tetrachloroplatinate(II) (K$_2$PtCl$_4$, 99.9%), sulfuric acid (H$_2$SO$_4$, 98%), and hydrazine hydrate (N$_2$H$_4$·H$_2$O, 85%) were acquired from Aladdin Reagent Database Inc. (Shanghai, China). Commercial Pt nanoparticles from Johnson Matthey Corporation (Pt–JM nanoparticles) were obtained from Hesen Electric Co., Ltd (Shanghai, China).

Preparation of the PEI functionalized Pt superstructures (Pt-SSs@PEI)

To synthesize Pt-SSs@PEI, a 5 mM water-soluble Pt^{II}–PEI complex solution was first prepared by dissolving 20 mg of K$_2$PtCl$_4$ and 430 mg of PEI in 10 mL of deionized water under vigorous stirring.[24,35] When the solution pH was adjusted to 8.0, the Pt^{II}–PEI complex solution was placed in a water bath set at 80 °C for 30 min. Then, 1 mL of N$_2$H$_4$·H$_2$O solution was added to the Pt^{II}–PEI complex solution and maintained for 15 h at 80 °C under static conditions. Finally, the black Pt-SSs@PEI precipitate was separated by centrifugation and washed several times with deionized water.

Electrochemical measurements

Cyclic voltammetry (CV), chronopotentiometry, chronoamperometry, and linear sweep voltammetry (LSV) measurements were performed using a three electrode cell on a CHI660D electrochemical workstation with a Gamry Rotating disk electrode (RDE, 710 rotating disk electrode) at 30 ± 1 °C. A saturated calomel electrode served as the reference electrode, and a carbon rod served as the counter electrode. The working electrode was prepared according to previous reports.[25,36] The catalyst was dispersed in a mixture of deionized water, isopropanol, and Nafion ($V/V/V$ = 8/2/0.05) to form an ink. Then, 10 μL of the catalyst ink (2 mg mL^{-1}) was deposited on the polished glassy carbon working electrode with 5 mm diameter and then air-dried under ambient conditions. All the potentials were presented with reference to a reversible hydrogen electrode (RHE), which was obtained using the following equation ($E_{RHE} = E_{SCE} + 0.059$ pH + 0.242). CV measurements were carried out in a N$_2$-saturated 0.5 M H$_2$SO$_4$ solution at 50 mV s^{-1}. The HER activity of the electrocatalyst was investigated with LSV measurements in a N$_2$-saturated 0.5 M H$_2$SO$_4$ solution at 2 mV s^{-1} and at a rotation speed of 1600 rpm with a 95% iR drop correction. The stability of the electrocatalyst was investigated with chronoamperometry, chronopotentiometry, and repeating CV scan techniques under stirring conditions. Chronoamperometry measurements were carried out in a N$_2$-saturated 0.5 M H$_2$SO$_4$ solution at the potential of −0.05 V for 7200 s under constant magnetic stirring. Chronopotentiometry measurements were performed in a N$_2$-saturated 0.5 M H$_2$SO$_4$ solution at a constant current density of 10 mA cm^{-2} under constant magnetic stirring. Repeating CV scans were performed in a N$_2$-purged 0.5 M H$_2$SO$_4$ solution for 10 000 potential cycles at 50 mV s^{-1} between 0 and 1.2 V. All electrochemical data were the average value of the eight measurements.

Instruments

The morphology of the sample was characterized with a scanning electron microscope (FE-SEM, SU8020), a high resolution transmission electron microscope (HRTEM, Tecnai G2 F20), an atomic force microscope (AFM), and a high angle annular dark-field scanning transmission electron microscope (HAADF-STEM, Tecnai G2 F20) with energy dispersive X-ray spectrometry (EDX). The crystal structure of the sample was determined

with an X-ray diffractometer (XRD, DX-2700). The surface composition and surface charge of the sample were investigated with X-ray photoelectron spectroscopy (XPS, AXIS ULTRA, XPS specific binding energies (BEs) were calibrated to C 1s = 284.6 eV). A thermogravimetric analyzer (TGA, TA Q600SDT) and a Malvern Zetasizer Nano ZS90 system were also used. The reduction process of the Pt^{II}–PEI complex was monitored by ultraviolet and visible spectroscopy (UV-vis, Shimadzu UV2600U). The thickness of the PEI on the Pt surface was measured with a VAS ellipsometer (Ellip-SR-II).

Results and discussion

Characterization of the Pt-SSs@PEI

A simple aqueous chemical reduction approach was developed to synthesize Pt-SSs@PEI with high yield. Herein, the Pt-SSs@PEI were readily achieved by reducing K_2PtCl_4 with $N_2H_4 \cdot H_2O$ in the presence of PEI (see Experimental section for details). The morphology and architecture of the Pt-SSs@PEI were investigated by scanning electron microscopy (SEM, Fig. 1A) and transmission electron microscopy (TEM, Fig. 1B). SEM and TEM images reveal that Pt superstructures with hierarchical and branched morphologies are the predominant products. An individual Pt superstructure with an edge length of approximately 80 nm consists of many interconnected branches (Fig. 1C). For an individual Pt superstructure, the HAADF-STEM image shows that the brightness at the centre is higher than that at the edge (Fig. 1D), indicating that the Pt superstructures are not 2D nanotriangles but rather 3D nanotetragons. The AFM height profile of the individual Pt superstructure reveals that the height at the centre is higher than that at the edge (Fig. 1E), confirming its 3D tetragonal morphology. The selected area electron diffraction (SAED) pattern exhibits concentric rings consisting of discrete bright diffraction dots (Fig. 1F), indicating high crystallinity. The HRTEM image at the branch edge shows that the lattice fringes have an interval distance of *ca.* 0.226 nm (Fig. 1G), corresponding to the Pt(111) crystal planes. Meanwhile, the HRTEM image at the branch bifurcation shows that the lattice fringes are perfect and continuous in the same direction (Fig. 1H), indicating an autocatalytic reduction growth mechanism.[37,38]

XRD was performed to determine the structure and phase of the Pt-SSs@PEI (Fig. 2A). As observed, Pt-SSs@PEI display four broad diffraction peaks at $2\theta = 39.8°$, $46.3°$, $67.5°$, and $81.3°$, corresponding to the (111), (200), (220) and (311) plane reflections of Pt, which match the data of the *fcc* Pt crystal denoted by the International Centre for Diffraction Data (JCPDS 04-0802) well. XPS measurements were performed to survey the surface chemical composition and oxidation states.[39] The elements of C, N, and Pt are detected and the N/Pt atomic ratio is measured to be 1 : 18 (Fig. S1 in ESI†). The Pt 4f peaks are located at 75.7 and 72.4 eV (Fig. 2B), which directly correspond to the binding energies of Pt $4f_{7/2}$ and Pt $4f_{5/2}$, respectively. The Pt 4f XPS spectrum can be further deconvoluted into metallic Pt and oxidized Pt. According to the peak areas, the ratio of metallic Pt is calculated to be 87.3%, revealing a high reduction ratio in our synthesis. Meanwhile, the appearance of a strong N 1s signal
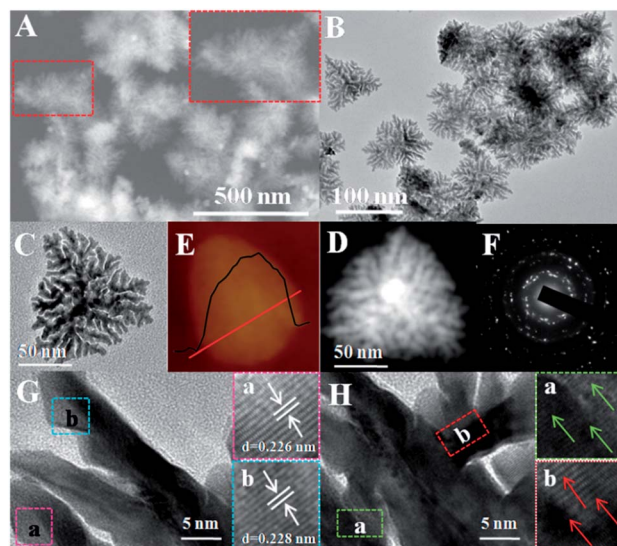

Fig. 1 Morphological and structural characterization of Pt-SSs@PEI. (A) Large-area SEM image and (B) large-area TEM image of Pt-SSs@PEI. (C) TEM image, (D) HAADF-STEM image, (E) AFM image, and (F) SAED pattern of an individual Pt-SS@PEI; (G) HRTEM image at the Pt-SSs@PEI branch edge. Inset: Magnified HRTEM images taken from regions a and b marked by squares in 1G, respectively. (H) HRTEM image at the Pt-SSs@PEI branch bifurcation. Inset: Magnified HRTEM images taken from regions a and b marked by squares in 1H, respectively.

indicates the adsorption of PEI on the surface of the Pt-SSs@PEI due to a strong Pt–N interaction (Fig. 2C).[27,28] Indeed, the zeta potential of the Pt-SSs@PEI is measured to be +44 mV due to the
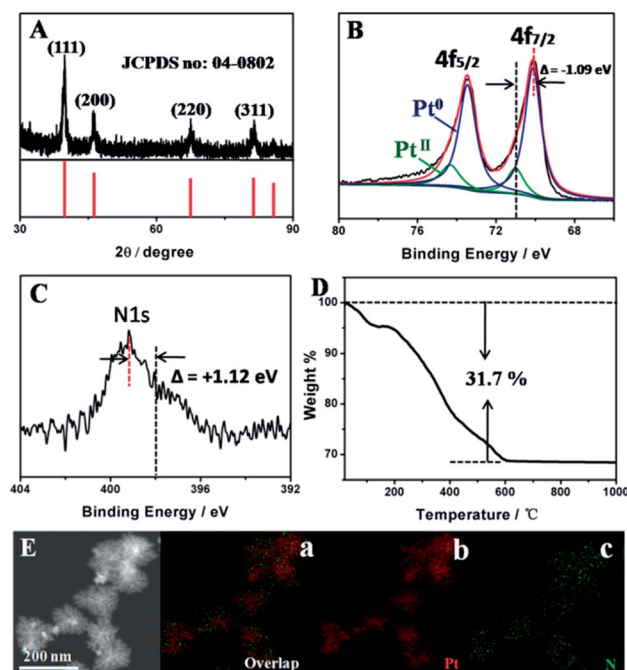

Fig. 2 The surface physical/chemical properties of Pt-SSs@PEI. (A) XRD pattern, (B) Pt 4f XPS spectrum, and (C) N 1s XPS spectrum of Pt-SSs@PEI. (D) TGA curve of Pt-SSs@PEI at a heating rate of 10 °C min^{-1} under a nitrogen atmosphere. (E) HAADF-STEM image and EDX elemental maps of an individual Pt-SS@PEI.
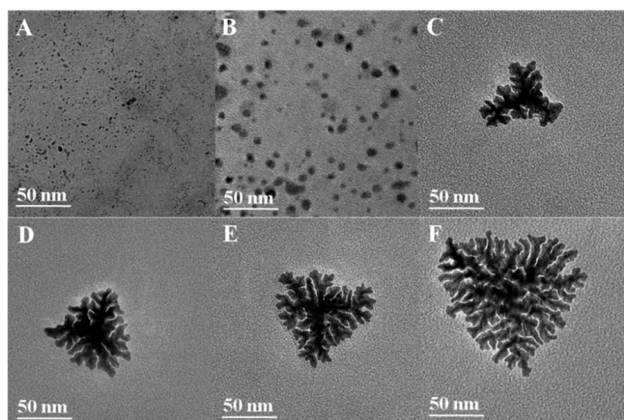
Fig. 3 TEM images of the reaction intermediates collected at (A) 3, (B) 4, (C) 6, (D) 8, (E) 10, and (F) 15 h, respectively.
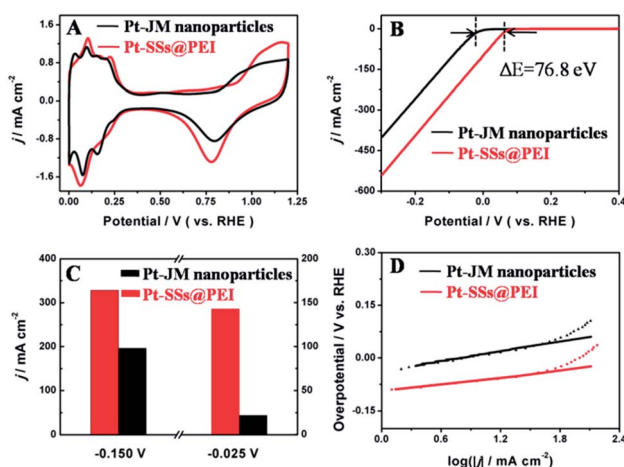

Fig. 4 Electrocatalytic activity for the HER. (A) CV curves of Pt-SSs@PEI and commercial Pt–JM nanoparticles in a N$_2$-saturated 0.5 M H$_2$SO$_4$ solution at 50 mV s^{-1}. (B) LSV curves of Pt-SSs@PEI and commercial Pt–JM nanoparticles for the HER in a N$_2$-purged 0.5 M H$_2$SO$_4$ solution at 2 mV s^{-1} and a rotating rate of 1600 rpm. (C) HER current densities at the Pt-SSs@PEI and the commercial Pt–JM nanoparticles at −0.025 V and −0.150 V, respectively. (D) Tafel plots for the HER at Pt-SSs@PEI and commercial Pt–JM nanoparticles in a N$_2$-saturated 0.5 M H$_2$SO$_4$ solution.
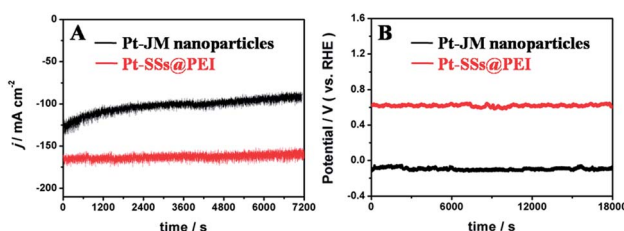

Fig. 5 Durability of Pt-SSs@PEI for the HER. (A) Chronoamperometry of Pt-SSs@PEI and commercial Pt–JM nanoparticles in a N$_2$-saturated 0.5 M H$_2$SO$_4$ solution for 10 000 s at −50 mV potential. (B) Chronopotentiometry curves of Pt-SSs@PEI and commercial Pt–JM nanoparticles in a N$_2$-saturated 0.5 M H$_2$SO$_4$ solution at a constant current density of 10 mA cm^{-2}.
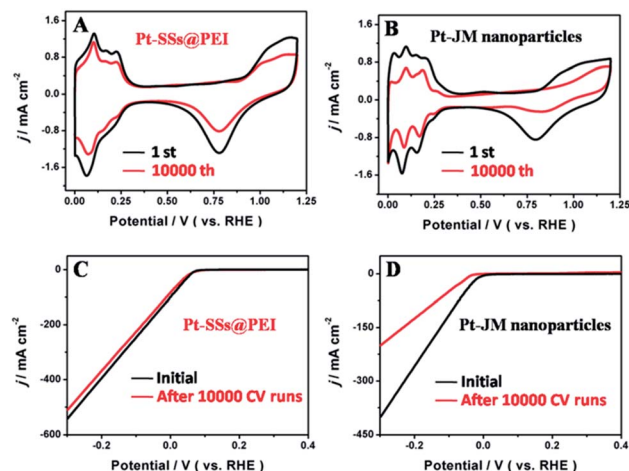

Fig. 6 The self-stability of Pt-SSs@PEI. CV curves of (A) Pt-SSs@PEI and (B) commercial Pt–JM nanoparticles before and after repeating CV scans in a N$_2$-purged 0.5 M H$_2$SO$_4$ solution at 50 mV s^{-1}. LSV polarization curves of (C) Pt-SSs@PEI and (D) commercial Pt–JM nanoparticles before and after repeating CV scans in a N$_2$-purged 0.5 M H$_2$SO$_4$ solution at 2 mV s^{-1} and with a rotating rate of 1600 rpm.

protonation of the –NH$_2$ groups on PEI, further confirming the binding of PEI onto the Pt surface. Compared to standard Pt 4f BE and N 1s BE values, the Pt 4f BE and the N 1s BE of the Pt-SSs@PEI exhibit a negative shift (1.09 eV) and a positive shift (1.12 eV), respectively, confirming the strong interaction between Pt atoms and –NH$_2$ groups (Fig. 2B and C). Thermogravimetric analysis indicates that the mass fraction of PEI in the Pt-SSs@PEI is *ca.* 31.7% (Fig. 2D). To further verify the adsorption of PEI on the Pt surface, EDX mapping measurements were performed (Fig. 2E). Pt and N element patterns are very similar, indicating the homogeneous phase of the Pt-SSs@PEI. Furthermore, the perfect match between the emerging positions of Pt and N elements confirms the uniform distribution of PEI on the Pt surface.

Formation mechanism of the Pt-SSs@PEI

As is well known, the morphology of nanocrystals relates to nucleation and crystal growth rates. According to the lowest energy principle, the generation of Pt-SSs@PEI is not preferred thermodynamically. Thus, the growth process under kinetic control is necessary for the generation of Pt-SSs@PEI. Due to the strong coordination ability of the –NH$_2$ groups, PEI can interact with K$_2$PtCl$_4$ to generate a light yellow PEI–Pt^{II} complex.[40] The generation of the PEI–Pt^{II} complex sharply decreases the reduction potential of Pt^{II} species (Fig. S2 in ESI†), which may effectively slow the reduction rate of the Pt^{II} precursor. Time-dependent ultraviolet and visible spectroscopy (UV-vis) absorption spectra show that the reduction of the PEI–Pt^{II} complex by N$_2$H$_4$·H$_2$O is completed within 15 h (Fig. S3 in ESI†). This slow reaction rate is also confirmed by the digital photographs of the actual reaction system at different times (Fig. S4 in ESI†). The colour of the solution changes from faint yellow to pale gray at 3 h, and finally to black at 15 h. Obviously, such a slow reduction rate allows the kinetically controlled

synthesis of Pt nanocrystals. Indeed, in the absence of PEI, the Pt^{II} precursor can be rapidly reduced by $N_2H_4 \cdot H2O$ within 3 min (Fig. S5 in ESI†), in which the Pt nanocrystals aggregate extensively (Fig. S6 in ESI†). This fact further indicates that the slow reduction rate is necessary for the generation of Pt-SSs@PEI. Meanwhile, the zeta potential of Pt aggregates is measured to be +2.4 mV, which in turn confirms that the high zeta potential of the Pt-SSs@PEI (+44 mV) originates from the protonation of amino groups in PEI.

To understand the formation mechanism of the Pt-SSs@PEI in detail, TEM images were taken at different reaction times during Pt-SSs@PEI growth (Fig. 3). At the initial stage, large numbers of ultrafine and monodispersed Pt seeds generate (Fig. 3A). Subsequently, the freshly-generated Pt atoms continuously deposit onto the original Pt nuclei through homogeneous nucleation, growing into the twinned nanoparticles (Fig. 3B). As the reaction proceeds, the twinned nanoparticles evolve into tetragonal Pt superstructures with branched morphology and the branching degree of intermediates increases with reaction time (Fig. 3C–E). By further increasing the reaction time to 15 h, the Pt-SSs@PEI with tetragonal, hierarchical, and branched morphologies are finally formed (Fig. 3F). Time-dependent TEM images show that the degree of branching of the intermediates is strongly related to the reaction time. Meanwhile, the lattice fringes at the bifurcations are continuous (Fig. 1H). Thus, a slow nucleation and a fast autocatalytic reduction of Pt^{II} species on freshly-generated Pt intermediates are responsible for the formation of Pt superstructures with branched morphology. Additionally, the branched molecular structure of the PEI molecule contributes to the high branching degree of the Pt-SSs@PEI. When polyallylamine with a straight-chain structure was used to replace PEI with a branched structure, ill-defined Pt nanodendrites with branched structures were obtained under the same experimental conditions (Fig. S7 in ESI†). This fact indicates that the branching degree of the Pt nanostructures relates to the branching degree of the polymeric amine. Due to the generation of the polymeric amine–Pt^{II} complex, Pt^{II} species fix on the carbon chain of the polymeric amine. After reduction occurs, the newly generated Pt crystal nuclei tend to combine in the carbon chain direction. Thus, the high degree of branching of the polymeric amine facilitates the generation of Pt nanostructures with a high branching degree. After further increasing the reaction time to 25 h, the TEM image shows that the morphology of the Pt-SSs@PEI remains constant (Fig. S8 in ESI†). This fact indicates the Pt-SSs@PEI have good thermal stability.

Electrocatalytic activity for the HER

To evaluate the electrochemical performance of the Pt-SSs@PEI and Pt–JM nanoparticles, CV tests were first performed in a N_2-saturated 0.5 M H_2SO_4 solution at 50 mV s^{-1} (Fig. 4A). Both CV curves display similar contours of hydrogen adsorption/desorption and formation/reduction of Pt oxide. According to the change in hydrogen adsorption between 0 V and 0.35 V, the actual electrochemical active surface area (ECSA) of the Pt-

SSs@PEI and commercial Pt–JM nanoparticles are calculated to be 22.4 m^2 g^{-1} and 19.9 m^2 g^{-1}, respectively. Although PEI molecules exist at the Pt surface, the ECSA of the Pt-SSs@PEI is still bigger than that of the commercial Pt–JM nanoparticles, indicating that the PEI adlayers have only taken up some of the Pt sites. After the removal of PEI in the Pt-SSs@PEI by hypochlorite oxidation, the ECSA of the Pt-SSs is measured to be 30.2 m^2 g^{-1} (Fig. S9 in ESI†), indicating that the surface coverage of the PEI adlayers on the Pt-SSs is ca. 25.8%. Due to the steric effect (i.e., the highly branched molecular structure of PEI), PEI only forms loosely packed adlayers on the Pt-SS surface,[41] which effectively retains most of the Pt sites for the electrochemical reaction.

The HER performance of the Pt-SSs@PEI and commercial Pt–JM nanoparticles was evaluated with the LSV technique (Fig. 4B). The current densities of the HER were normalized by the geometric area of the working electrode. The onset potential (E_{onset}) of the HER was defined at the potential value at a current density of 10 mA cm^{-2}. The E_{onset} value (+64.6 mV vs. RHE) at the Pt-SSs@PEI is much higher than that (-12.2 mV vs. RHE) at commercial Pt–JM nanoparticles, revealing improved electrocatalytic activity for the HER. Very importantly, the E_{onset} value (+64.6 mV vs. RHE) at the Pt-SSs@PEI is much higher than the theoretical Nernst value (0 mV vs. RHE) of the HER, which also surpasses all previously reported values[3,6,10,42–53] (Table S1†). According to the reaction equation of the HER in acidic media ($2H^+ + 2e^- \rightarrow H_2$), the H^+ concentration at the electrode/solution interface determines the E_{onset} value of the HER. Thus, the proton enrichment at the Pt surface will undoubtedly increase the E_{onset} value of the HER. The aforementioned XPS, zeta potential, and EDX maps results have confirmed the binding of PEI to the Pt-SSs@PEI. In acidic media, the $-NH_2$ groups in the PEI adlayers will completely protonate to generate $-NH_3^+$, which may result in proton enrichment at the Pt surface. Optical ellipsometry is a convenient and precise method for determining the adlayer thickness on the solid surface. The thickness of the PEI adlayer on the Pt surface is measured to be 5.69 nm with ellipsometry. By combining the thickness of the PEI adlayer, the mass fraction of the PEI adlayer in the Pt-SSs@PEI, and the ECSA of the Pt-SSs, the H^+ concentration on the Pt-SSs@PEI is estimated to be 5.1×10^2 M, much higher than the H^+ concentration in the 0.5 M H_2SO_4 solution. Thus, we reasonably state that the proton enrichment in the Pt-SSs@PEI is responsible for the super activity of the Pt-SSs@PEI for the HER. After the removal of PEI, the E_{onset} value of the HER at the Pt-SSs decreases to -10.4 mV (Fig. S10 in ESI†), which in turn confirms the proton enrichment results in the activity enhancement of the Pt-SSs@PEI for the HER in acidic media. In addition, the HER current at the Pt-SSs without PEI is higher than that at the Pt aggregates, indicating that the 3D morphology of the Pt-SSs also contributes to the HER activity enhancement (Fig. S11 in ESI†).

To further evaluate the HER performance of the Pt-SSs@PEI and commercial Pt–JM nanoparticles, the cathodic current density was provided at a certain potential (Fig. 4C). The current densities for the HER at the Pt-SSs@PEI are about 143 mA cm^{-2} and 328 mA cm^{-2} at -0.025 V and -0.075 V potentials, which

are 1.67 and 6.50 times larger than those at the commercial Pt–JM nanoparticles under the same potentials. The results further demonstrate that the Pt-SSs@PEI have excellent electrocatalytic activity for the HER in acidic media. The Tafel slope of the HER at the electrocatalyst was commonly used to evaluate the reaction kinetics of the HER. The Tafel slope could be obtained by the Tafel equation ($\eta = a + b \log j$, where j represents the current density, b represents the Tafel slope, a represents the intercept, and η represents the overpotential).[51,54] A smaller Tafel slope usually stands for faster HER kinetics. For the HER in acidic media, there are three possible reactions.[55] The first step is related to the discharge of the proton ($H_3O^+ + e^- \rightarrow H_{ad} + H_2O$, $b \approx 120$ mV dec^{-1}), which is called the Volmer reaction. The following two possible steps are proposed as the Heyrovsky reaction ($H_{ad} + H_3O^+ + e^- \rightarrow H_2 + H_2O$, $b \approx 40$ mV) and the Tafel reaction ($H_{ad} + H_{ad} \rightarrow H_2$, $b \approx 30$ mV).[44,56] The Tafel slope for the HER at the Pt-SSs@PEI is calculated to be about 28 mV dec^{-1}, which is very close to that (33 mV dec^{-1}) at the commercial Pt–JM nanoparticles (Fig. 4D), indicating that the HER at both the Pt-SSs@PEI and commercial Pt–JM nanoparticles obeys the Tafel reaction mechanism under the present experimental conditions. This result indicates that the control over the interface structure of Pt nanocrystals has no direct effect on the reaction mechanism of the HER.

Durability of the Pt-SSs@PEI for the HER

The electrocatalytic stabilities of the Pt-SSs@PEI and the commercial Pt–JM nanoparticles were evaluated with chronoamperometry and chronopotentiometry techniques in a N$_2$-purged 0.5 M H$_2$SO$_4$ solution. The chronoamperometry measurements reveal that the Pt-SSs@PEI only undergo a slight loss of current density after running for 7200 s at 0.05 V potential whereas commercial Pt–JM nanoparticles have an obvious decay in current density (Fig. 5A), indicating that Pt-SSs@PEI exhibit improved electrocatalytic stability compared to commercial Pt–JM nanoparticles. The stability enhancement was further confirmed by chronopotentiometry tests. At a constant current density of 10 mA cm^{-2}, the Pt-SSs@PEI only generate a 15 mV potential shift after 18 000 s whereas commercial Pt–JM nanoparticles have a 28 mV potential shift (Fig. 5B), confirming that Pt-SSs@PEI have better electrocatalytic stability than commercial Pt–JM nanoparticles.

To understand the excellent stability of the Pt-SSs@PEI for the HER, the self-stability of the Pt-SSs@PEI was investigated by repeating CV scans between 0 and 1.2 V at 50 mV s^{-1} in a N$_2$-purged 0.5 M H$_2$SO$_4$ solution and the results were further compared with those of commercial Pt–JM nanoparticles. After 10 000 potential cycles, the Pt-SSs@PEI retained 96.7% of the initial ECSA value (Fig. 6A) whereas commercial Pt–JM nanoparticles lost more than 40% of the initial ECSA value (Fig. 6B). The TEM image shows that the Pt-SSs@PEI do not show an obvious morphological change after long-term CV cycling (Fig. S12 in ESI†), which is ascribed to the interconnected structure and high crystallinity of the Pt-SSs@PEI that can effectively suppress the Ostwald ripening phenomenon.[32,57–63] After 10 000 CV cycles, the HER performance of the Pt-SSs@PEI

and the commercial Pt–JM nanoparticles was detected by LSV. As can be observed, the HER performance of the Pt-SSs@PEI remains constant in a perfect way (Fig. 6C) while that of the commercial Pt–JM nanoparticles shows an obvious performance decay for the HER (Fig. 6D). Based on the above discussion, we can draw the conclusion that the outstanding self-stability of the Pt-SSs@PEI is responsible for the excellent durability of the Pt-SSs@PEI for the HER.

Conclusions

In summary, we have developed a facile one-pot chemical reduction strategy to synthesize Pt-SSs@PEI in the presence of PEI with a branched molecular structure. Experimental results show that the branched molecular structure of PEI favors the formation of highly branched Pt nanocrystals. The relationship between the morphology of the products and the spatial structure of the surfactant opens up a new synthesis strategy for highly branched nanocrystals. Quite significantly, Pt-SSs@PEI exhibit excellent eletrocatalytic activity for the HER, including a very high onset reduction potential of +64.6 mV and a very big current density of 328 mA cm^{-2} at −150 mV potential. The protonation of –NH$_2$ groups in the PEI adlayers effectively increases the local H$^+$ concentration at the electrode/solution interface, which results in an extraordinarily high activity of the Pt-SSs@PEI for the HER in acidic media. Meanwhile, the 3D interconnected structure of the Pt-SSs@PEI imparts the Pt-SSs@PEI with excellent self-stability, resulting in long-term stability for the HER. This work provides a combinational morphology/interface-engineering strategy for developing highly active Pt-based HER electrocatalysts in acidic media, which may be used in other electrochemical reactions involving H$^+$ participation.

Conflicts of interest

There are no conflicts to declare.

Acknowledgements

Notes and references

1 D. Yoon, B. Seo, J. Lee, K. S. Nam, B. Kim, S. Park, H. Baik, S. H. Joo and K. Lee, *Energy Environ. Sci.*, 2016, **9**, 850–856.

2 M. Chhetri, S. Maitra, H. Chakraborty, U. V. Waghmare and C. Rao, *Energy Environ. Sci.*, 2016, **9**, 95–101.

3 P. Wang, X. Zhang, J. Zhang, S. Wan, S. Guo, G. Lu, J. Yao and X. Huang, *Nat. Commun.*, 2017, **8**, 14580.

4 D. V. Esposito, S. T. Hunt, A. L. Stottlemyer, K. D. Dobson, B. E. McCandless, R. W. Birkmire and J. G. Chen, *Angew. Chem., Int. Ed.*, 2010, **49**, 9859–9862.

5 H. H. Wei, Z. J. Yang, Y. L. Min, J. C. Fan and Q. J. Xu, *Part. Part. Syst. Charact.*, 2017, **34**, 1600200.

6 N. Cheng, S. Stambula, D. Wang, M. N. Banis, J. Liu, A. Riese, B. Xiao, R. Li, T.-K. Sham, L.-M. Liu, G. A. Botton and X. Sun, *Nat. Commun.*, 2016, **7**, 13638.

7 L. Zhu, H. Lin, Y. Li, F. Liao, Y. Lifshitz, M. Sheng, S.-T. Lee and M. Shao, *Nat. Commun.*, 2016, **7**, 12272.

8 S. Bai, C. Wang, M. Deng, M. Gong, Y. Bai, J. Jiang and Y. Xiong, *Angew. Chem., Int. Ed.*, 2014, **53**, 12120–12124.

9 N. Marković, B. Grgur and P. Ross, *J. Phys. Chem. B*, 1997, **101**, 5405–5413.

10 N. Du, C. Wang, X. Wang, Y. Lin, J. Jiang and Y. Xiong, *Adv. Mater.*, 2016, **28**, 2077–2084.

11 A. Ponrouch, S. Garbarino, E. Bertin, C. Andrei, G. A. Botton and D. Guay, *Adv. Funct. Mater.*, 2012, **22**, 4172–4181.

12 B. Genorio, D. Strmcnik, R. Subbaraman, D. Tripkovic, G. Karapetrov, V. R. Stamenkovic, S. Pejovnik and N. M. Markovic, *Nat. Mater.*, 2010, **9**, 998–1003.

13 B. Genorio, R. Subbaraman, D. Strmcnik, D. Tripkovic, V. R. Stamenkovic and N. M. Markovic, *Angew. Chem., Int. Ed.*, 2011, **50**, 5468–5472.

14 M. N. Cao, D. S. Wu, S. Y. Gao and R. Cao, *Chem.–Eur. J.*, 2012, **18**, 12978–12985.

15 Z. Y. Zhou, X. W. Kang, Y. Song and S. W. Chen, *Chem. Commun.*, 2012, **48**, 3391–3393.

16 C. Susut, D.-J. Chen, S.-G. Sun and Y. J. Tong, *Phys. Chem. Chem. Phys.*, 2011, **13**, 7467–7474.

17 Y. J. Tong, *Chem. Soc. Rev.*, 2012, **41**, 8195–8209.

18 G. Fu, K. Wu, J. Lin, Y. Tang, Y. Chen, Y. Zhou and T. Lu, *J. Phys. Chem. C*, 2013, **117**, 9826–9834.

19 X. Gao, Y. Li, Q. Zhang, S. Li, Y. Chen and J.-M. Lee, *J. Mater. Chem. A*, 2015, **3**, 12000–12004.

20 Y. Tan, C. Xu, G. Chen, N. Zheng and Q. Xie, *Energy Environ. Sci.*, 2012, **5**, 6923–6927.

21 J. Snyder, T. Fujita, M. Chen and J. Erlebacher, *Nat. Mater.*, 2010, **9**, 904–907.

22 M. Escudero-Escribano, M. E. Zoloff Michoff, E. P. M. Leiva, N. M. Marković, C. Gutiérrez and Á. Cuesta, *ChemPhysChem*, 2011, **12**, 2230–2234.

23 D. Strmcnik, M. Escudero-Escribano, K. Kodama, V. R. Stamenkovic, A. Cuesta and N. M. Markovic, *Nat. Chem.*, 2010, **2**, 880–885.

24 G. Fu, K. Wu, X. Jiang, L. Tao, Y. Chen, J. Lin, Y. Zhou, S. Wei, Y. Tang, T. Lu and X. Xia, *Phys. Chem. Chem. Phys.*, 2013, **15**, 3793–3802.

25 F.-M. Li, X.-Q. Gao, S.-N. Li, Y. Chen and J.-M. Lee, *NPG Asia Mater.*, 2015, **7**, e219.

26 G. Fu, X. Jiang, M. Gong, Y. Chen, Y. Tang, J. Lin and T. Lu, *Nanoscale*, 2014, **6**, 8226–8234.

27 G.-R. Xu, B. Wang, J.-Y. Zhu, F.-Y. Liu, Y. Chen, J.-H. Zeng, J.-X. Jiang, Z.-H. Liu, Y.-W. Tang and J.-M. Lee, *ACS Catal.*, 2016, **6**, 5260–5267.

28 G.-R. Xu, J. Bai, L. Yao, Q. Xue, J.-X. Jiang, J.-H. Zeng, Y. Chen and J.-M. Lee, *ACS Catal.*, 2017, 452–458.

29 J.-X. Feng, H. Xu, S.-H. Ye, G. Ouyang, Y.-X. Tong and G.-R. Li, *Angew. Chem., Int. Ed.*, 2017, **56**, 8120–8124.

30 J. X. Feng, L. X. Ding, S. H. Ye, X. J. He, H. Xu, Y. X. Tong and G. R. Li, *Adv. Mater.*, 2015, **27**, 7051–7057.

31 H.-l. Liu, F. Nosheen and X. Wang, *Chem. Soc. Rev.*, 2015, **44**, 3056–3078.

32 A. Oh, H. Baik, D. S. Choi, J. Y. Cheon, B. Kim, H. Kim, S. J. Kwon, S. H. Joo, Y. Jung and K. Lee, *ACS Nano*, 2015, **9**, 2856–2867.

33 Z. Niu, D. Wang, R. Yu, Q. Peng and Y. Li, *Chem. Sci.*, 2012, **3**, 1925–1929.

34 F. Zaera, *Chem. Soc. Rev.*, 2013, **42**, 2746–2762.

35 X. Qiu, G. Fu, Y. Zhao, Y. Tang, Y. Chen and T. Lu, *J. Mater. Chem. A*, 2013, **1**, 14874–14878.

36 D. Zhao and B. Q. Xu, *Angew. Chem.*, 2006, **118**, 5077–5081.

37 J. Chen, B. Lim, E. P. Lee and Y. Xia, *Nano Today*, 2009, **4**, 81–95.

38 X. Zhong, Y. Feng, I. Lieberwirth and W. Knoll, *Chem. Mater.*, 2006, **18**, 2468–2471.

39 F. F. Tao, S. Zhang, L. Nguyen and X. Zhang, *Chem. Soc. Rev.*, 2012, **41**, 7980–7993.

40 G.-R. Xu, F.-Y. Liu, Z.-H. Liu and Y. Chen, *J. Mater. Chem. A*, 2015, **3**, 21083–21089.

41 J. Bai, C.-L. Fang, Z.-H. Liu and Y. Chen, *Nanoscale*, 2016, **8**, 2875–2880.

42 S. Wang, X. Gao, X. Hang, X. Zhu, H. Han, W. Liao and W. Chen, *J. Am. Chem. Soc.*, 2016, **138**, 16236–16239.

43 P. Wang, K. Jiang, G. Wang, J. Yao and X. Huang, *Angew. Chem., Int. Ed.*, 2016, **55**, 12859–12863.

44 Y. Mi, L. Wen, Z. Wang, D. Cao, H. Zhao, Y. Zhou, F. Grote and Y. Lei, *Catal. Today*, 2016, **262**, 141–145.

45 E. Gottlieb, M. Kopec, M. Banerjee, J. Mohin, D. Yaron, K. Matyjaszewski and T. Kowalewski, *ACS Appl. Mater. Interfaces*, 2016, **8**, 21531–21538.

46 F. Ren, H. Lu, H. Liu, Z. Wang, Y. Wu and Y. Li, *J. Mater. Chem. A*, 2015, **3**, 23660–23663.

47 Y. Shen, A. C. Lua, J. Xi and X. Qiu, *ACS Appl. Mater. Interfaces*, 2016, **8**, 3464–3472.

48 Z. Cao, Q. Chen, J. Zhang, H. Li, Y. Jiang, S. Shen, G. Fu, B.-a. Lu, Z. Xie and L. Zheng, *Nat. Commun.*, 2017, **8**, 15131.

49 L. Wang, Y. Zhu, Z. Zeng, C. Lin, M. Giroux, L. Jiang, Y. Han, J. Greeley, C. Wang and J. Jin, *Nano Energy*, 2017, **31**, 456–461.

50 Y. Wang, L. Chen, X. Yu, Y. Wang and G. Zheng, *Adv. Energy Mater.*, 2017, **7**, 1601390.

51 B. Zhang, H. Zhu, M. Zou, X. Liu, H. Yang, M. Zhang, W. Wu, J. Yao and M. Du, *J. Mater. Sci.*, 2017, **52**, 8207–8218.

52 M. Tavakkoli, N. Holmberg, R. Kronberg, H. Jiang, J. Sainio, E. I. Kauppinen, T. Kallio and K. Laasonen, *ACS Catal.*, 2017, **7**, 3121–3130.

53 L. Ji, J. Wang, S. Zuo and Z. Cheno, *J. Phys. Chem. C*, 2017, **121**, 8923–8930.

54 J. Kye, M. Shin, B. Lim, J.-W. Jang, I. Oh and S. Hwang, *ACS Nano*, 2013, **7**, 6017–6023.

55 B. Conway and B. Tilak, *Electrochim. Acta*, 2002, **47**, 3571–3594.

56 H. Lv, Z. Xi, Z. Chen, S. Guo, Y. Yu, W. Zhu, Q. Li, X. Zhang, M. Pan, G. Lu, S. Mu and S. Sun, *J. Am. Chem. Soc.*, 2015, **137**, 5859–5862.

57 B. Y. Xia, H. B. Wu, Y. Yan, X. W. Lou and X. Wang, *J. Am. Chem. Soc.*, 2013, **135**, 9480–9485.

58 B. Y. Xia, H. B. Wu, N. Li, Y. Yan, X. W. Lou and X. Wang, *Angew. Chem., Int. Ed.*, 2015, **54**, 3797–3801.

59 L. Ma, C. Wang, M. Gong, L. Liao, R. Long, J. Wang, D. Wu, W. Zhong, M. J. Kim, Y. Chen, Y. Xie and Y. Xiong, *ACS Nano*, 2012, **6**, 9797–9806.

60 Y. Li, H. Zhang, T. Xu, Z. Lu, X. Wu, P. Wan, X. Sun and L. Jiang, *Adv. Funct. Mater.*, 2015, **25**, 1737–1744.

61 B. Y. Xia, W. T. Ng, H. Bin Wu, X. Wang and X. W. Lou, *Angew. Chem., Int. Ed.*, 2012, **51**, 7213–7216.

62 Z. Niu, D. Wang, R. Yu, Q. Peng and Y. Li, *Chem. Sci.*, 2012, **3**, 1925–1929.

63 S. Sun, G. Zhang, D. Geng, Y. Chen, R. Li, M. Cai and X. Sun, *Angew. Chem., Int. Ed.*, 2011, **50**, 422–426.